Monthly Notices
of the
ROYAL ASTRONOMICAL SOCIETY

MNRAS **524,** 4418–4430 (2023) https://doi.org/10.1093/mnras/stad2156
Advance Access publication 2023 July 21

# An investigation of non-canonical mixing in red giant stars using APOGEE $^{12}$C/$^{13}$C ratios observed in open cluster stars

Caroline McCormick[1★] Steven R. Majewski,[1] Verne V. Smith,[2,3] Christian R. Hayes,[4] Katia Cunha,[3,5,6] Thomas Masseron,[7,8] Achim Weiss[9] Matthew Shetrone,[10] Andrés Almeida,[1] Peter M. Frinchaboy,[11] Domingo Aníbal García-Hernández[7] and Christian Nitschelm[12]

[1]*Department of Astronomy, University of Virginia, 530 McCormick Road, Charlottesville, VA 22904, USA*
[2]*NSF's National Optical-Infrared Astronomy Research Laboratory, 950 North Cherry Avenue, Tucson, AZ 85719, USA*
[3]*Institut d'Astrophysique de Paris, UMR7095 CNRS, Sorbonne Université, 98bis Bd Arago, F-75014 Paris, France*
[4]*Herzberg Astronomy and Astrophysics Research Centre, 5071 West Saanich Road, Victoria, BC V9E 2E7, Canada,*
[5]*Observatório Nacional, 77 Rua General José Cristino, Rio de Janeiro 20921-400, Brazil*
[6]*Steward Observatory, University of Arizona, 933 North Cherry Avenue, Tucson, AZ 85721, USA*
[7]*Instituto de Astrofísica de Canarias, E-38205 La Laguna, Tenerife, Spain*
[8]*Departamento de Astrofísica, Universidad de La Laguna, E-38206 La Laguna, Tenerife, Spain*
[9]*Max-Planck-Institut für Astrophysik, Karl-Schwarzschild-Str. 1, D-85748 Garching, Germany*
[10]*University of California Observatories, University of California Santa Cruz, Santa Cruz, CA 95064, USA*
[11]*Department of Physics & Astronomy, Texas Christian University, Fort Worth, TX 76129, USA*
[12]*Centro de Astronomía (CITEVA), Universidad de Antofagasta, Avenida Angamos 601, Antofagasta 1270300, Chile*

Accepted 2023 July 10. Received 2023 May 27; in original form 2022 October 17

## ABSTRACT

Standard stellar evolution theory poorly predicts the surface abundances of chemical species in low-mass, red giant branch (RGB) stars. Observations show an enhancement of p–p chain and CNO cycle products in red giant envelopes, which suggests the existence of non-canonical mixing that brings interior burning products to the surface of these stars. The $^{12}$C/$^{13}$C ratio is a highly sensitive abundance metric used to probe this mixing. We investigate extra RGB mixing by examining: (1) how $^{12}$C/$^{13}$C is altered along the RGB, and (2) how $^{12}$C/$^{13}$C changes for stars of varying age and mass. Our sample consists of 43 red giants, spread over 15 open clusters from the Sloan Digital Sky Survey's APOGEE DR17, that have reliable $^{12}$C/$^{13}$C ratios derived from their APOGEE spectra. We vetted these $^{12}$C/$^{13}$C ratios and compared them as a function of evolution and age/mass to the standard mixing model of stellar evolution, and to a model that includes prescriptions for RGB thermohaline mixing and stellar rotation. We find that the observations deviate from standard mixing models, implying the need for extra mixing. Additionally, some of the abundance patterns depart from the thermohaline model, and it is unclear whether these differences are due to incomplete observations, issues inherent to the model, our assumption of the cause of extra mixing, or any combination of these factors. Nevertheless, the surface abundances across our age/mass range clearly deviate from the standard model, agreeing with the notion of a universal mechanism for RGB extra mixing in low-mass stars.

**Key words:** convection – instabilities – stars: abundances – stars: atmospheres – stars: interiors – open clusters and associations: general.

## 1 INTRODUCTION

A thorough knowledge of the chemical evolution of stellar populations, galaxies, and the universe as a whole is only achievable with a complete, or at least sound, understanding of stellar evolution through all major developmental phases for all initial stellar masses. Particularly, in regards to the chemical evolution of galaxies and their interstellar media (ISM), it is essential to understand how the observed elemental abundance patterns in stars relate to their internal nucleosynthetic processes, and the eventual yields they contribute to the ISM through chemical enrichment.

One specific area of uncertainty is the array of mixing processes that take place in the interiors of evolved, low- and intermediate-mass stars,[1] and how these processes affect surface abundances. Traditional stellar evolution models (i.e. models where only convection is responsible for interior mixing) predict that the surface abundances in low- and intermediate-mass, evolved stars should remain unchanged after the first dredge-up at the beginning of the red giant branch (RGB), until subsequent alterations take place during the asymptotic giant branch (AGB) phase. However, observations of upper RGB and horizontal branch stars (e.g. Sneden, Pilachowski

---

[1] Here, low-mass stars are ∽0.8–2 $M_\odot$ stars, and intermediate-mass stars are ∽2–8 $M_\odot$.

★ E-mail: uea6uk@virginia.edu

Published by Oxford University Press on behalf of Royal Astronomical Society

& Vandenberg 1986; Gilroy 1989; Gratton et al. 2000; Smiljanic et al. 2009; Tautvaišienė et al. 2010, 2013; Drazdauskas et al. 2016; Takeda et al. 2019; Charbonnel et al. 2020) have shown that certain surface abundances are in fact altered during this period of stellar evolution, which suggests the existence of a non-canonical mixing process at work.

A variety of physical mechanisms, such as cool bottom processing (Boothroyd, Sackmann & Wasserburg 1995; Wasserburg, Boothroyd & Sackmann 1995; Boothroyd & Sackmann 1999; Sackmann & Boothroyd 1999), stellar rotation (Sweigart & Mengel 1979; Charbonnel 1995; Chanamé, Pinsonneault & Terndrup 2005; Palacios et al. 2006), and magnetic fields (Busso et al. 2007; Denissenkov, Pinsonneault & MacGregor 2009), have been proposed to have at least some level of contribution to this non-canonical mixing on the upper RGB. However, there is still no definitive consensus on the exact conditions and processes at work that cause the extra mixing. One of the more popular physical mechanisms to which extra mixing is attributed (and one of the mechanisms to which we compare our data) is a double-diffusive instability, generically referred to as a thermohaline instability in the literature (Stern 1960). Charbonnel & Zahn (2007) identified that this double-diffusive instability is the first instability to occur and alter the interior mean molecular weight ($\mu$) profile, due to the growing inverse-$\mu$ gradient at this phase of evolution. Furthermore, this instability occurs naturally in low-mass and less massive intermediate-mass ($\lesssim$2.2 $M_\odot$; Charbonnel & Lagarde 2010) stars on the RGB. Stellar rotation is the second mechanism to which we compare our data, and it is also known to complicate the surface abundances in RGB stars. This stellar rotation during the main sequence causes the diffusion of material within a star, thereby changing the internal abundance profiles of species such as $^{12}$C and $^{13}$C. While these composition changes are not significant enough to produce noticeable changes at the surface of the star during the main sequence, the effects do show up during the first dredge-up, when the envelope makes contact with the mixed interior regions (e.g. Palacios et al. 2003; Charbonnel & Lagarde 2010).

During the first dredge-up, the convective envelope of the star reaches deep into regions that have been chemically modified by hydrogen burning and mixes to the surface matter enriched in by-products of the proton-proton (p-p) chains and carbon-nitrogen-oxygen (CNO) cycle, such as $^{3}$He, $^{13}$C, and $^{14}$N, and depleted in $^{12}$C and $^{7}$Li, thereby diluting the initial surface abundances of the star. The first dredge-up homogenizes the chemical composition of the red giant envelope and leaves behind a chemical discontinuity at the border between the farthest inward extent of the envelope during the first dredge-up, and the radiative layer just outside the hydrogen-burning shell (HBS). Further along the RGB, the star reaches the so-called luminosity bump, where the outward-extending HBS reaches the chemical discontinuity and causes a temporary dip in the stellar luminosity. It is at this point that the proposed thermohaline instability sets in to eventuate an extra mixing episode that further alters the surface abundances and produces some of the unusual patterns that have been observed.

Thermohaline instability is initiated by the $^{3}$He ($^{3}$He, 2p)$^{4}$He p–p chain reaction occurring in the outer HBS. This reaction decreases $\mu$ in the burning region, since more particles result from this reaction than the number of particles that were present initially. Therefore, $\mu$ increases outwards, producing an inverse $\mu$ gradient locally. The higher-$\mu$ material sinks, and it is eventually mixed with its surroundings. As a result of this process, products of CNO burning such as $^{13}$C and $^{14}$N located in surrounding regions are transported throughout the thermohaline unstable region. Provided there is enough $^{3}$He to sustain this inverse $\mu$ gradient, the thermohaline unstable region will eventually come into contact with the convective envelope, causing further mixing of the burning products to the surface.

Because extra mixing on the RGB is directly connected to changes in surface abundances of p–p and CNO species, one way to probe the effects of the mixing is to compare the abundances and ratios of certain atomic species, such as $^{12}$C/$^{13}$C or [C/N], between otherwise similar stars that are in evolutionary stages before, during, and after this mixing episode is expected to occur (e.g. Szigeti et al. 2018). Comparing these observations to models including prescriptions for the physical mechanism(s) (e.g. thermohaline instability, rotation), that could cause the extra mixing will help us better understand the interior mixing conditions in these stars. The present analysis relies on the $^{12}$C/$^{13}$C ratio because it shows a heightened sensitivity to mixing. The ratio typically drops from $\gtrsim$70 to $\backsim$20 during the first dredge-up, and to $\backsim$10 after extra mixing. Also, when compared to [C/N], the $^{12}$C/$^{13}$C ratio is thought to be a more powerful tool to use in constraining extra mixing (see Lagarde et al. 2019).

In this work, we employ data from Data Release 17 (DR17; Abdurro'uf et al. 2022) of the Sloan Digital Sky Survey IV's (SDSS-IV; Blanton et al. 2017) Apache Point Observatory Galactic Evolution Experiment (APOGEE; Majewski et al. 2017) and its value added catalogues (VACs), which contain open cluster membership evaluations for $\backsim$26 000 stars and derived $^{12}$C/$^{13}$C ratios for $\backsim$120 000 red giants. With this data, we obtain a sample of 43 confirmed open cluster red giant members with homogeneously derived $^{12}$C/$^{13}$C ratios. Adopting open cluster stars for our analyses allows us to assign reliable ages[2] and initial masses for the stars belonging to each cluster. Our goal is to gain insight into the overall importance and cause of extra mixing, as well as its effects in stars of varying age and mass on the RGB. Specifically, we study how $^{12}$C/$^{13}$C changes over time and as a function of age and mass, and compare these observations to models including the effects of thermohaline extra mixing and stellar rotation, for which models are publicly available for testing (Lagarde et al. 2012).

This paper is organized as follows: Section 2 outlines the APOGEE data used and the justification of the selection criteria applied to obtain our final sample of open cluster red giants. We present the evolution of the $^{12}$C/$^{13}$C ratio along the RGB and the $^{12}$C/$^{13}$C ratio as a function of age and mass in Section 3. In Section 4, we discuss the broader impact of our results with respect to stellar evolution and extra mixing model predictions, and finally, in Section 5, we summarize and draw conclusions from our work.

## 2 DATA

We utilize spectroscopic data from SDSS DR17 (Abdurro'uf et al. 2022) – the final data release of SDSS-IV (Blanton et al. 2017) collaboration. This data release contains all of the data taken as part of the APOGEE and APOGEE-2 surveys (Majewski et al. 2017), which used the two APOGEE spectrographs (Wilson et al. 2019): APOGEE-N on the Sloan 2.5-meter Telescope in New Mexico (Gunn et al. 2006) with an auxiliary feed from the NMSU 1-meter telescope (Holtzman, Harrison & Coughlin 2010) and APOGEE-S on the 2.5-meter du Pont Telescope (Bowen & Vaughan 1973) at Las Campanas Observatory in Chile. Targeting for the APOGEE survey is described in Zasowski et al. (2013), while that for the APOGEE-2 survey is described in Zasowski et al. (2017), Beaton et al. (2021), and Santana

---

[2] It is assumed that stars belonging to an open cluster are all formed at the same time, and therefore, are of the same age.

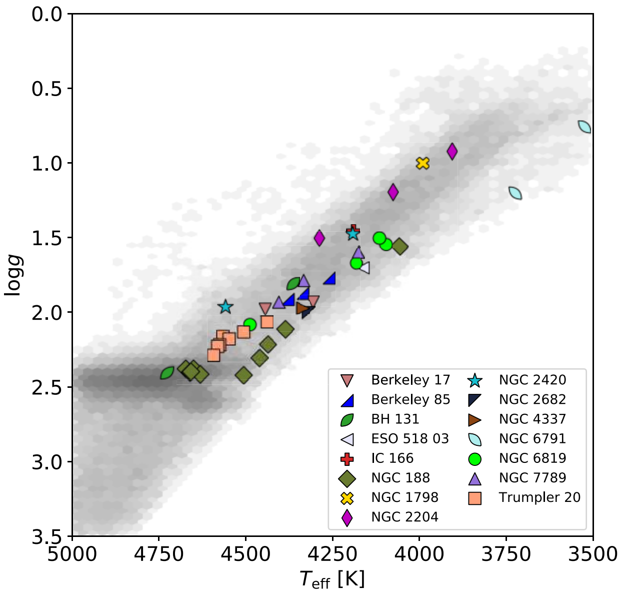

**Figure 1.** The $T_{\mathrm{eff}}$ - log $g$ diagram of all cluster stars in our final sample (*coloured symbols*). The background grey scale shows the relative density of stars in the BAWLAS VAC with derived $^{12}$C/$^{13}$C.

et al. (2021). Additionally, Frinchaboy et al. (2013) and Donor et al. (2018) give targeting information for the open clusters observed in APOGEE. The data reduction pipeline for APOGEE is described in Nidever et al. (2015) and in Holtzman et al. (2015) for the APOGEE spectra taken with the 1-meter telescope.

The APOGEE Stellar Atmospheric Parameters and Chemical Abundances Pipeline (ASPCAP; García Pérez et al. 2016), which is based on the FERRE code written by Allende Prieto et al. (2006), obtains stellar atmospheric parameters and chemical abundances by finding the best match in a library of synthetic spectra. For DR17, ASPCAP uses a grid of MARCS stellar atmospheres (Gustafsson et al. 2008; Jönsson et al. 2020), and an $H$-band line list from Smith et al. (2021), which is an update of the Shetrone et al. (2015) line list.

For the present work, the $^{12}$C/$^{13}$C ratios were derived from APOGEE DR17 spectra and stellar parameters from ASPCAP using the Brussels Automatic Code for Characterizing High accUracy Spectra (BACCHUS; Masseron, Merle & Hawkins 2016); these ratios are reported in the BACCHUS Analysis of Weak-Lines in APOGEE Spectra (BAWLAS) VAC which contains data for ∽120,000 red giants (Hayes et al. 2022). The stars analysed in the BAWLAS VAC, including our final sample cluster stars, can be seen in the $T_{\mathrm{eff}}$ - log $g$ diagrams in Figs 1 and 2. We next describe the cuts and requirements applied to the full APOGEE data set to derive our final sample of red giants and their stellar parameters.

### 2.1 Cluster membership cuts

We first sought red giants that are members of Galactic open clusters because ages and initial masses for these clusters and stars can be reliably inferred. To verify cluster membership, we used the Open Cluster Chemical Abundance and Mapping (OCCAM) survey (Donor et al. 2018; Donor et al. 2020; Myers et al. 2022), which provides cluster membership probabilities for 26 699 stars in 153 open clusters observed in APOGEE. Of the 153 open clusters, we only considered the best clusters as denoted by the quality flag given in OCCAM being set to 1 or 2 (see Donor et al. 2020 for definition). Additionally, we required that each cluster have at least five reliably determined member stars identified in OCCAM to provide a greater chance at having well-populated clusters in our analyses, and to have a higher confidence in the membership analysis for each cluster.

We then analysed the membership probability for each star, supposedly belonging to each of these clusters. To be a cluster member according to the OCCAM survey, a star must have a radial velocity (RV), metallicity ([Fe/H]), and proper motion (PM) within three standard deviations of the cluster mean values. In other words, the ‘RV Prob’, ‘[Fe/H] Prob’, and ‘PM Prob’ reported values must be >0.01.

From the combination of these open cluster membership criteria, the initial OCCAM sample of 26 699 stars is reduced to 1196 reliable cluster members belonging to 43 clusters.

### 2.2 BAWLAS VAC Carbon measurement criteria

Due to the difficulty of measuring the weak lines that are used in determining the $^{12}$C/$^{13}$C ratio, the BAWLAS VAC includes trustworthy $^{12}$C/$^{13}$C ratios for 52 855 of its stars and $^{12}$C/$^{13}$C lower, or $^{13}$C upper, limits for 49 252 stars. For a star to be included in our final sample, we required that the star must have a non-limit $^{12}$C/$^{13}$C value. Combining this criterion with the verified open cluster member stars from the OCCAM survey, there are 212 stars belonging to 24 open clusters.

### 2.3 Age and mass determinations

Because we are investigating the $^{12}$C/$^{13}$C ratio as a function of age, we further limited the sample of stars to only include stars in clusters with previously determined ages. We surveyed the literature for open cluster ages, seeking to find a set of estimates where most, if not all, cluster ages in our sample are determined in a consistent manner. No single source was found that had reported ages for all of the clusters arising from the Section 2.1 OCCAM membership and Section 2.2 $^{12}$C/$^{13}$C cuts. However, we minimized the variety of sources by adopting cluster ages from three sources: Cantat-Gaudin et al. (2020), Bossini et al. (2019), and Dias et al. (2002). Cantat-Gaudin et al. (2020) was our default cluster age source, as they provide consistently derived and generally reliable cluster ages for a large number of clusters. We used Bossini et al. (2019) and Dias et al. (2002) when ages from Cantat-Gaudin et al. (2020) were either untrustworthy (NGC 6791; Brogaard et al. 2021) or unavailable (BH 131). We found that 15 of the 24 open clusters have ages reported by these sources, resulting in a sample of 49 red giant stars in these 15 particular clusters.

Table 1 lists the final collection of clusters represented in our sample, along with the number of stars in each cluster with reliable $^{12}$C/$^{13}$C ratios and $^{12}$C/$^{13}$C limits, the DR17 mean cluster metallicity ([Fe/H]) derived from ASPCAP, the age of each cluster, the literature source for each age, and the initial stellar mass for RGB stars in each cluster. These masses were determined from MIST isochrones (Choi et al. 2016; Dotter 2016; Paxton et al. 2011, 2013, 2015, 2018), which adopt solar-scaled abundances. We input the cluster’s age and mean [Fe/H] and adopted the initial mass of a star at the terminal age main sequence, which is at equivalent evolutionary point 454, as the red giant initial mass for each cluster. We acquired masses for RGB stars in all 15 clusters with reported ages, so no further cuts are made to the sample here.

### 2.4 Spectral fit cuts

The $^{12}$C/$^{13}$C ratios reported in the BAWLAS VAC were determined using the BACCHUS code to fit CO and CN lines in eight windows centred on 15641.7 Å, 16121.4 Å, 16323.4 Å, 16326.0 Å, 16327.3 Å, 16530.0 Å, 16741.2 Å, and 16744.7 Å. This approach allows for the

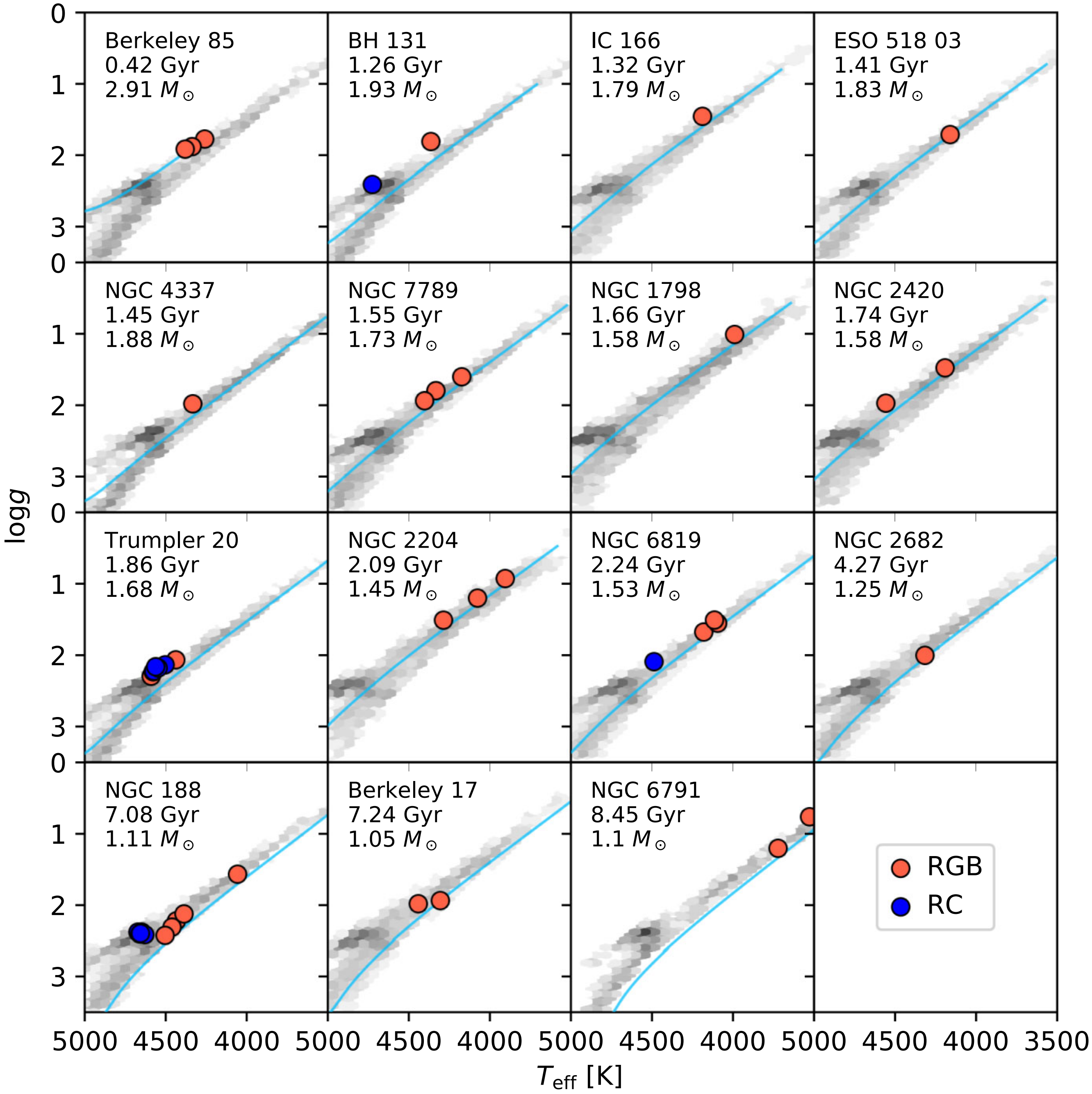

**Figure 2.** The $T_{\rm eff}$ - log $g$ diagram of our final sample stars (*circles*) in each cluster along with the best-matching cluster isochrone (*light blue curves*), generated using the MESA Isochrones & Stellar Tracks (MIST) models (Choi et al. 2016; Dotter 2016; Paxton et al. 2011, 2013, 2015, 2018). Typical errors in log $g$ are 0.02 dex and in $T_{\rm eff}$ are 3–8 K. *Blue circles* correspond to red clump stars that have ignited core He-burning, while *orange circles* correspond to stars on the RGB. The background grey scale shows the density of stars in the BAWLAS VAC with derived $^{12}$C/$^{13}$C and [Fe/H] within 0.03 dex of the cluster mean [Fe/H].

efficient processing of such a large data set, however, there is always the possibility that some spectra are affected by noise and/or have poorly fit features. To ensure that our observed $^{12}$C/$^{13}$C-age/mass relations are accurate, we visually inspected all eight spectral fits for all 49 stars in our sample and manually vetted the $^{12}$C/$^{13}$C ratios, updating the values as necessary.

For each star, we characterized the fit to the CO or CN line in each of the eight spectral windows as a ‘measurement’ (i.e. the line is acceptably well fit), a ‘limit’ (i.e. the line is decently fit but could be better), or a ‘non-measurement’ (i.e. the fit is not representative of the observed spectrum). These categories were assigned after several inspections of each spectral fit, since defining what is a ‘good’ fit versus a ‘bad’ fit can be somewhat subjective. Factors such as: (1) how well the synthetic spectra matched the shape of the observed spectra, and (2) whether the synthetic spectra were noticeably shifted above or below the observed spectral feature were considered in this process. Both of these factors could act to artificially increase or decrease the derived $^{12}$C/$^{13}$C, so careful consideration was given to identify these biases. Examples of measurement, limit, and non-measurement spectral fits are shown in Fig. 3.

**Table 1.** Open clusters with at least one red giant with a reliable $^{12}$C/$^{13}$C ratio derived from the BAWLAS VAC. Also listed are the cluster mean metallicities ([Fe/H]) and standard error, the initial stellar mass of stars at the cluster main sequence turn off, the adopted cluster age, and the literature source for the age of each cluster.

| Cluster name | Number of stars | Number of BAWLAS $^{12}$C/$^{13}$C limit stars | [Fe/H] | Mass ($M_\odot$) | Age (Gyr) | Age source |
|---|---|---|---|---|---|---|
| Berkeley 17 | 2 | 2 | – 0.17 ± 0.01 | $1.05^{+0.08}_{-0.11}$ | $7.24^{+2.99}_{-2.11}$ | Cantat-Gaudin et al. (2020) |
| Berkeley 85 | 4 | 1 | 0.10 ± 0.01 | $2.91^{+0.43}_{-0.61}$ | $0.42^{+0.17}_{-0.12}$ | Cantat-Gaudin et al. (2020) |
| BH 131 | 2 | 3 | 0.09 ± 0.01 | 1.93 | 1.26 | Dias et al. (2002)[1] |
| ESO 518 03 | 1 | 2 | 0.03 ± 0.01 | $1.83^{+0.21}_{-0.30}$ | $1.41^{+0.59}_{-0.41}$ | Cantat-Gaudin et al. (2020) |
| IC 166 | 1 | 0 | – 0.16 ± 0.01 | $1.79^{+0.22}_{-0.30}$ | $1.32^{+0.54}_{-0.41}$ | Cantat-Gaudin et al. (2020) |
| NGC 188 | 10 | 6 | 0.06 ± 0.01 | $1.11^{+0.08}_{-0.11}$ | $7.08^{+2.92}_{-2.07}$ | Cantat-Gaudin et al. (2020) |
| NGC 1798 | 1 | 3 | – 0.35 ± 0.01 | $1.58^{+0.19}_{-0.26}$ | $1.66^{+0.68}_{-0.49}$ | Cantat-Gaudin et al. (2020) |
| NGC 2204 | 3 | 6 | – 0.36 ± 0.01 | $1.45^{+0.16}_{-0.23}$ | $2.09^{+0.86}_{-0.61}$ | Cantat-Gaudin et al. (2020) |
| NGC 2420 | 2 | 5 | – 0.26 ± 0.01 | $1.58^{+0.18}_{-0.26}$ | $1.74^{+0.71}_{-0.51}$ | Cantat-Gaudin et al. (2020) |
| NGC 2682 | 1 | 18 | – 0.03 ± 0.01 | $1.25^{+0.11}_{-0.15}$ | $4.27^{+1.76}_{-1.25}$ | Cantat-Gaudin et al. (2020) |
| NGC 4337 | 1 | 3 | 0.19 ± 0.01 | $1.88^{+0.21}_{-0.28}$ | $1.45^{+0.59}_{-0.43}$ | Cantat-Gaudin et al. (2020) |
| NGC 6791 | 4 | 0 | 0.28 ± 0.02 | $1.10^{+0.001}_{-0.001}$ | $8.45^{+0.04}_{-0.04}$ | Bossini et al. (2019) |
| NGC 6819 | 4 | 13 | – 0.02 ± 0.02 | $1.53^{+0.16}_{-0.22}$ | $2.24^{+0.92}_{-0.66}$ | Cantat-Gaudin et al. (2020) |
| NGC 7789 | 4 | 24 | – 0.05 ± 0.01 | $1.73^{+0.19}_{-0.28}$ | $1.55^{+0.64}_{-0.45}$ | Cantat-Gaudin et al. (2020) |
| Trumpler 20 | 9 | 2 | 0.08 ± 0.01 | $1.68^{+0.17}_{-0.25}$ | $1.86^{+0.77}_{-0.54}$ | Cantat-Gaudin et al. (2020) |

[1] No cluster age uncertainty was provided.

Once the fits to each star's eight spectral features were characterized as well fit or not, we computed the final $^{12}$C/$^{13}$C ratios for each star. The BACCHUS code derives a separate $^{12}$C/$^{13}$C value based on the fit for each of the eight spectral features, so we computed a given star's total $^{12}$C/$^{13}$C by averaging the ratio values provided for each well-fit line. All spectral fits falling into the 'measurement' or 'limit' categories, such as the top and middle panels in Fig. 3, were used to determine the star's final $^{12}$C/$^{13}$C value. We report the standard deviation of these $^{12}$C/$^{13}$C values from well-fit spectral lines as the $^{12}$C/$^{13}$C error. We note that this error calculation often underestimates the true error, especially for stars with fewer well-fit lines that produce a measurement, and it does not take into account systematic errors in the measurement and modelling processes (see Hayes et al. 2022).

Overall, we found only three instances of stars that had generally poor fits for most of their eight spectral features. The APOGEE IDs (and clusters) for these three stars are 2M19212437+3735402 (NGC 6791), 2M23571013+5647167 (NGC 7789), and 2M12392699−6036052 (Trumpler 20), and their $^{12}$C/$^{13}$C ratios are reported as $^{12}$C/$^{13}$C lower limits.

While any combination of the eight spectral features could give the final $^{12}$C/$^{13}$C value, we required that each star must have well-fit 15641.7 Å and 16530.0 Å lines as a means to bring some level of standardization to the process. These lines were chosen because they were the most common lines with generally good fits in our sample, and stars displaying generally questionable fits were often lacking good fits for at least one of these two lines. Stars that display poor fits for at least one of these two lines have their $^{12}$C/$^{13}$C value shown as a lower limit. The following three stars were excluded from the sample after imposing this condition: 2M20190397+3745002 (Berkeley 85), 2M19213635+3739445 (NGC 6791), and 2M12402480−6043101 (Trumpler 20). Adopting this last criterion brings our final sample to 43 stars with $^{12}$C/$^{13}$C ratio measurements and six stars providing $^{12}$C/$^{13}$C limits. We adopt the manually vetted $^{12}$C/$^{13}$C values for the subsequent analysis in this paper.

The results of this spectral analysis can be seen in Table 2, which gives the stellar parameters, our manually vetted $^{12}$C/$^{13}$C values, OCCAM cluster membership probabilities, and evolutionary states (RGB or red clump) for all stars that were determined to have reliable $^{12}$C/$^{13}$C ratios. Table 3 includes the final sample stars with $^{12}$C/$^{13}$C measurements and those stars with $^{12}$C/$^{13}$C limits. This table displays the BAWLAS VAC $^{12}$C/$^{13}$C values as well as our manually determined $^{12}$C/$^{13}$C values for easy comparison between the two analyses. Additionally, the table lists the lines we used in determining the ratio for each star.

## 3 RESULTS

### 3.1 Evolution of $^{12}$C/$^{13}$C with $\log g$

A crucial test for understanding the nature of extra mixing on the RGB is to observe how the $^{12}$C/$^{13}$C ratio evolves with time, or equivalently surface gravity ($\log g$), on the RGB and red clump (RC), and compare this evolution to models that take into account an extra mixing mechanism. Fig. 4 presents the $^{12}$C/$^{13}$C evolution with $\log g$ for our open cluster stars (orange and blue circles), separated into each cluster. Additionally, the $^{12}$C/$^{13}$C limit stars, determined in the BAWLAS VAC and through our manual spectral fit examination are shown as dark grey arrows, and the light grey points represent stars in the BAWLAS VAC with [Fe/H], within 0.03 dex of the cluster mean [Fe/H]. In Fig. 4, we show models from Lagarde et al. (2012) (hereafter referred to as the 'Lagarde models'; dark grey, solid curves) that exhibit extra mixing effects caused by the combination of thermohaline instability and stellar rotation. Stars with mass above ∽2.2 $M_\odot$ at near-solar metallicity are not expected to reach the luminosity bump (e.g. Charbonnel & Lagarde 2010; Lagarde et al. 2019), so the model representing more massive stars (i.e. Berkeley 85) exhibit extra mixing effects due to stellar rotation rather than thermohaline instability. Less massive models exhibit a combined effect, but the thermohaline instability dominates extra mixing (e.g. Charbonnel & Lagarde 2010).

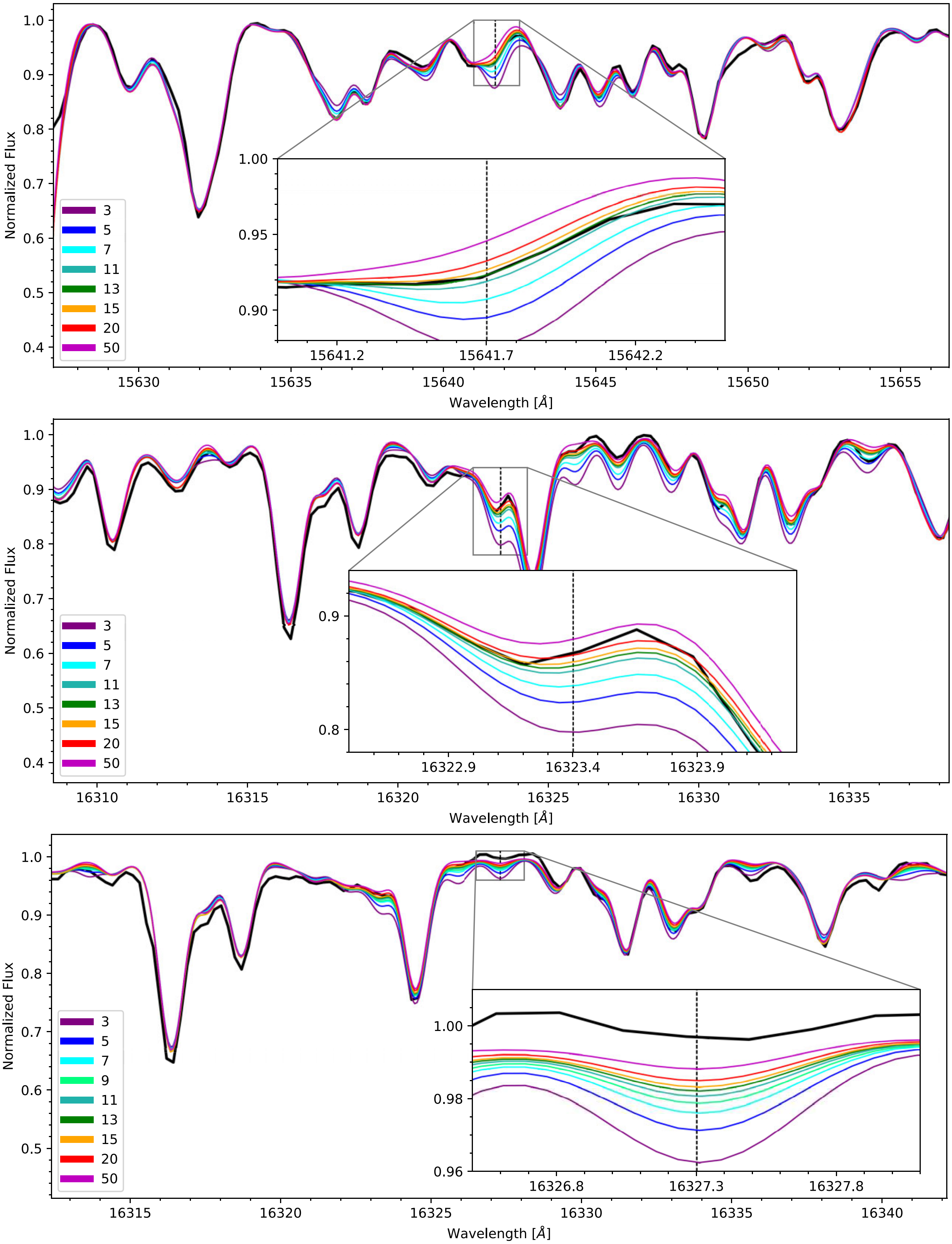

**Figure 3.** Examples of the models used by BACCHUS to fit spectral lines and derive $^{12}C/^{13}C$ ratios. Each *coloured line* represents a different value for $^{12}C/^{13}C$. The *black line* is the observed spectrum, and the vertical, *dashed line* marks the central wavelength of each spectral feature. *Top*: An example of a well-fit line characterized as a measurement where the dark green, $^{12}C/^{13}C = 13$ model provides the best fit for this line (star: 2M19413439+4017482; cluster: NGC 6819; average stellar $^{12}C/^{13}C = 13$). *Middle*: An example of a line characterized as a limit where the $^{12}C/^{13}C = 15$ (*orange*) and 20 (*red*) models provide the closest fits and slightly overestimate this star's $^{12}C/^{13}C$ (star: 2M19413439+4017482; cluster: NGC 6819; average stellar $^{12}C/^{13}C = 13$). *Bottom*: An example of a poor fit characterized as a non-measurement where the models clearly miss the spectrum and estimate an unreasonably large value (>50) for this particular line (star: 2M00571844+8510288; cluster: NGC 188; average stellar $^{12}C/^{13}C = 13$).

**Table 2.** Stellar parameters and manually vetted $^{12}$C/$^{13}$C ratios for all open cluster red giants (43) in the BAWLAS VAC that meet the selection criteria described in Section 2. Also listed are the RV, [Fe/H], and PM probabilities from OCCAM used to determine cluster membership for each star, and the evolutionary state for each star as reported in APOGEE.

| APOGEE ID | Cluster | $T_{\rm eff}$ (K) | log $g$ | [Fe/H] | $^{12}$C/$^{13}$C | RV prob | [Fe/H] prob | PM prob | Evol. state |
|---|---|---|---|---|---|---|---|---|---|
| 2M05203799+3034414 | Berkeley 17 | 4307 ± 6 | 1.93 ± 0.02 | −0.18 ± 0.01 | 13 ± 1 | 1.00 | 0.98 | 0.97 | RGB |
| 2M05203650+3030351 | Berkeley 17 | 4445 ± 7 | 1.98 ± 0.02 | −0.17 ± 0.01 | 11 ± 2 | 0.82 | 0.90 | 0.94 | RGB |
| 2M20183476+3740565 | Berkeley 85 | 4380 ± 6 | 1.91 ± 0.02 | 0.09 ± 0.01 | 16 ± 1 | 0.87 | 1.00 | 0.84 | RGB |
| 2M20183785+3743009 | Berkeley 85 | 4337 ± 6 | 1.87 ± 0.02 | 0.12 ± 0.01 | 17 ± 4 | 0.89 | 0.72 | 0.96 | RGB |
| 2M20184497+3744174 | Berkeley 85 | 4262 ± 5 | 1.77 ± 0.02 | 0.09 ± 0.01 | 14 ± 3 | 0.97 | 0.98 | 0.65 | RGB |
| 2M12260433−6324196 | BH 131 | 4365 ± 6 | 1.81 ± 0.02 | 0.09 ± 0.01 | 15 ± 2 | 0.87 | 0.95 | 0.99 | RGB |
| 2M12261653−6325258 | BH 131 | 4728 ± 8 | 2.41 ± 0.02 | 0.08 ± 0.01 | 12 ± 3 | 0.82 | 0.80 | 1.00 | RC |
| 2M16464504−2558201 | ESO 518 03 | 4163 ± 5 | 1.71 ± 0.02 | 0.03 ± 0.01 | 15 ± 3 | 0.98 | 0.91 | 0.85 | RGB |
| 2M01522919+6159381 | IC 166 | 4191 ± 6 | 1.45 ± 0.02 | −0.16 ± 0.01 | 14 ± 2 | 0.46 | 0.26 | 2.00 | RGB |
| 2M00455119+8518082 | NGC 188 | 4461 ± 6 | 2.31 ± 0.02 | 0.05 ± 0.01 | 16 ± 4 | 0.35 | 0.91 | 0.26 | RGB |
| 2M00441241+8509312 | NGC 188 | 4059 ± 5 | 1.56 ± 0.02 | −0.01 ± 0.01 | 17 ± 4 | 1.00 | 0.14 | 0.55 | RGB |
| 2M00320079+8511465 | NGC 188 | 4507 ± 6 | 2.42 ± 0.02 | 0.07 ± 0.01 | 13 ± 2 | 0.98 | 0.99 | 0.05 | RGB |
| 2M00465966+8513157 | NGC 188 | 4650 ± 7 | 2.38 ± 0.02 | 0.04 ± 0.01 | 17 ± 5 | 0.94 | 0.78 | 0.71 | RC |
| 2M00350924+8517169 | NGC 188 | 4673 ± 7 | 2.38 ± 0.02 | 0.05 ± 0.01 | 12 ± 1 | 0.98 | 0.91 | 0.12 | RC |
| 2M00571844+8510288 | NGC 188 | 4631 ± 7 | 2.41 ± 0.02 | 0.09 ± 0.01 | 13 ± 0.3 | 1.00 | 0.85 | 0.83 | RC |
| 2M00415197+8527070 | NGC 188 | 4661 ± 7 | 2.40 ± 0.02 | 0.08 ± 0.01 | 12 ± 1 | 0.92 | 0.93 | 0.32 | RC |
| 2M00445253+8514055 | NGC 188 | 4437 ± 6 | 2.22 ± 0.02 | 0.04 ± 0.01 | 10 ± 3 | 0.80 | 0.71 | 0.79 | RGB |
| 2M00581691+8540183 | NGC 188 | 4658 ± 7 | 2.40 ± 0.02 | 0.11 ± 0.01 | 7 ± 2 | 0.88 | 0.80 | 0.75 | RC |
| 2M00463920+8523336 | NGC 188 | 4387 ± 6 | 2.12 ± 0.02 | 0.04 ± 0.01 | 8 ± 2 | 0.98 | 0.74 | 0.03 | RGB |
| 2M05114795+4740258 | NGC 1798 | 3991 ± 5 | 1.01 ± 0.02 | −0.35 ± 0.01 | 15 ± 3 | 1.00 | 0.04 | 0.51 | RGB |
| 2M06153140−1842562 | NGC 2204 | 4077 ± 5 | 1.20 ± 0.02 | −0.35 ± 0.01 | 12 ± 1 | 0.88 | 0.41 | 0.78 | RGB |
| 2M06145845−1838429 | NGC 2204 | 4289 ± 6 | 1.50 ± 0.02 | −0.34 ± 0.01 | 11 ± 2 | 1.00 | 0.45 | 0.72 | RGB |
| 2M06153666−1846527 | NGC 2204 | 3907 ± 5 | 0.93 ± 0.02 | −0.38 ± 0.01 | 11 ± 1 | 0.98 | 0.07 | 0.94 | RGB |
| 2M07381507+2134589 | NGC 2420 | 4194 ± 6 | 1.48 ± 0.02 | −0.27 ± 0.01 | 10 ± 0.6 | 1.00 | 0.16 | 0.99 | RGB |
| 2M07382166+2133514 | NGC 2420 | 4559 ± 7 | 1.97 ± 0.02 | −0.25 ± 0.01 | 7 ± 0.1 | 0.99 | 0.34 | 0.02 | RGB |
| 2M08493465+1151256 | NGC 2682 | 4320 ± 6 | 2.00 ± 0.02 | −0.03 ± 0.01 | 8 ± 1 | 0.99 | 0.71 | 0.73 | RGB |
| 2M12240101−5807554 | NGC 4337 | 4336 ± 6 | 1.97 ± 0.02 | 0.19 ± 0.01 | 15 ± 4 | 1.00 | 0.81 | 0.78 | RGB |
| 2M19213390+3750202 | NGC 6791 | 3724 ± 4 | 1.20 ± 0.02 | 0.29 ± 0.01 | 13 ± 3 | 0.99 | 0.77 | 2.00 | RGB |
| 2M19211606+3746462 | NGC 6791 | 3527 ± 3 | 0.76 ± 0.02 | 0.23 ± 0.01 | 11 ± 1 | 0.98 | 0.10 | 0.61 | RGB |
| 2M19411705+4010517 | NGC 6819 | 4098 ± 5 | 1.55 ± 0.02 | −0.03 ± 0.01 | 15 ± 2 | 0.73 | 0.26 | 0.93 | RGB |
| 2M19411971+4023362 | NGC 6819 | 4116 ± 5 | 1.50 ± 0.02 | −0.06 ± 0.01 | 12 ± 2 | 0.82 | 0.05 | 2.00 | RGB |
| 2M19413439+4017482 | NGC 6819 | 4183 ± 5 | 1.67 ± 0.02 | 0.02 ± 0.01 | 13 ± 1 | 1.00 | 0.91 | 0.40 | RGB |
| 2M19412658+4011418 | NGC 6819 | 4488 ± 6 | 2.09 ± 0.02 | 0.00 ± 0.01 | 10 ± 2 | 0.98 | 0.65 | 0.28 | RC |
| 2M23570744+5641417 | NGC 7789 | 4177 ± 5 | 1.60 ± 0.02 | −0.06 ± 0.01 | 17 ± 3 | 0.99 | 0.77 | 0.94 | RGB |
| 2M23555312+5641203 | NGC 7789 | 4405 ± 6 | 1.93 ± 0.02 | −0.05 ± 0.01 | 11 ± 3 | 0.67 | 0.84 | 0.07 | RGB |
| 2M23581471+5651466 | NGC 7789 | 4335 ± 6 | 1.79 ± 0.02 | −0.04 ± 0.01 | 10 ± 0.9 | 0.49 | 0.80 | 0.72 | RGB |
| 2M12400451−6036566 | Trumpler 20 | 4440 ± 6 | 2.07 ± 0.02 | 0.06 ± 0.01 | 15 ± 2 | 0.66 | 0.28 | 0.90 | RGB |
| 2M12390411−6034001 | Trumpler 20 | 4548 ± 7 | 2.18 ± 0.02 | 0.09 ± 0.01 | 10 ± 1 | 1.00 | 1.00 | 0.94 | RC |
| 2M12400755−6035445 | Trumpler 20 | 4507 ± 6 | 2.13 ± 0.02 | 0.11 ± 0.01 | 10 ± 0.5 | 1.00 | 0.99 | 0.98 | RC |
| 2M12400260−6039545 | Trumpler 20 | 4580 ± 7 | 2.23 ± 0.02 | 0.10 ± 0.01 | 10 ± 2 | 0.92 | 0.99 | 0.99 | RC |
| 2M12391003−6038402 | Trumpler 20 | 4575 ± 7 | 2.22 ± 0.02 | 0.08 ± 0.01 | 11 ± 2 | 0.81 | 0.95 | 0.98 | RC |
| 2M12402949−6038518 | Trumpler 20 | 4593 ± 7 | 2.29 ± 0.02 | 0.08 ± 0.01 | 11 ± 1 | 0.86 | 0.86 | 0.93 | RGB |
| 2M12385807−6030286 | Trumpler 20 | 4566 ± 7 | 2.16 ± 0.02 | 0.07 ± 0.01 | 8 ± 2 | 0.81 | 0.48 | 0.65 | RC |

The Lagarde models were generated for discrete mass ($M$) and metallicity ([Fe/H]) values ranging from $M = 0.85$ to 6 $\mathrm{M}_{\odot}$ and [Fe/H] = -2.16 to 0. For comparison with the data, we chose the model with the closest mass and [Fe/H] values to each cluster (see Table 1 for the average, APOGEE-measured [Fe/H] and initial stellar mass from the MIST isochrone for each cluster). In Fig. 4, the Lagarde models encompass the time just after the end of the first dredge-up (the left-most black × symbol in each subplot at relatively high log $g$ and high $^{12}$C/$^{13}$C), until the early AGB (the lower horizontal sections at relatively low log $g$ and low $^{12}$C/$^{13}$C). Notably, the RGB luminosity bump (the middle × in each subplot) is clearly seen in most of the models at the point where there is a sudden large decrease in $^{12}$C/$^{13}$C (generally at log $g \approx 1.5$–2). Before this point, there are small changes in the surface $^{12}$C/$^{13}$C ratio due to rotation, however, after this point the HBS comes into contact with the envelope and thermohaline extra mixing alters the surface $^{12}$C/$^{13}$C ratio much more dramatically. Following the extra mixing dip, the models begin to flatten again just after the tip of the RGB (right-most × in each subplot in Fig. 4), as the star begins core He-burning on the horizontal branch.

In Fig. 4, the open cluster stars in our sample have been differentiated by colour to show stars at two evolutionary stages: orange circles represent stars on the RGB, either just before or currently undergoing extra mixing, and blue circles represent stars that have finished extra mixing on the RGB and are RC stars. The $^{12}$C/$^{13}$C limit stars are also classified as RGB or RC, as indicated by the shape of the grey arrow. We utilized the 'SPEC_RGB' and 'SPEC_RC' flags in the APOGEE 'PARAMFLAG' array to classify stellar evolutionary states in our sample. Originally, these flags were populated based on the work of Jönsson et al. (2020), which separated the stars in APOGEE based on evolutionary state to more accurately calibrate surface gravities for similar stars. Jönsson et al. (2020) categorized the APOGEE stars as dwarf, RGB, or RC based on a given star's spectroscopic log $g$ and $T_{\rm eff}$, total metallicity ([M/H]), and [C/N] values falling within a

**Table 3.** All stars (49) in our sample before vetting the $^{12}$C/$^{13}$C values. Listed for comparison are the $^{12}$C/$^{13}$C ratios determined in the BAWLAS VAC and those with manually vetted spectral fits of each star's lines. The 'Vetted lines' column shows the CN (i.e. 15641.7 Å and partially 16121.4 Å) and CO (i.e. partially 16121.4 Å and the remaining lines) lines we used in our calculation of $^{12}$C/$^{13}$C. The stars considered as $^{12}$C/$^{13}$C limits in our vetting process are denoted by > in the 'Manual $^{12}$C/$^{13}$C ' column.

| APOGEE ID | Cluster | Vetted lines (Å) | BAWLAS $^{12}$C/$^{13}$C | Manual $^{12}$C/$^{13}$C |
|---|---|---|---|---|
| 2M05203799+3034414 | Berkeley 17 | 15641.7, 16121.4, 16530.0 | 13 ± 2 | 13 ± 1 |
| 2M05203650+3030351 | Berkeley 17 | 15641.7, 16121.4, 16323.4, 16326.0, 16530.0, 16744.7 | 12 ± 4 | 11 ± 2 |
| 2M20183476+3740565 | Berkeley 85 | 15641.7, 16121.4, 16530.0 | 20 ± 5 | 16 ± 1 |
| 2M20183785+3743009 | Berkeley 85 | 15641.7, 16121.4, 16323.4, 16530.0 | 17 ± 6 | 17 ± 4 |
| 2M20190397+3745002 | Berkeley 85 | 16121.4, 16530.0 | 14 ± 2 | >15 ± 2 |
| 2M20184497+3744174 | Berkeley 85 | 15641.7, 16121.4, 16323.4, 16530.0 | 14 ± 3 | 14 ± 3 |
| 2M12260433−6324196 | BH 131 | 15641.7, 16121.4, 16530.0 | 15 ± 2 | 15 ± 2 |
| 2M12261653−6325258 | BH 131 | 15641.7, 16121.4, 16323.4, 16530.0, 16744.7 | 11 ± 2 | 12 ± 3 |
| 2M16464504−2558201 | ESO 518 03 | 15641.7, 16326.0, 16530.0, 16744.7 | 15 ± 4 | 15 ± 3 |
| 2M01522919+6159381 | IC 166 | 15641.7, 16121.4, 16530.0, 16744.7 | 12 ± 1 | 14 ± 2 |
| 2M00455119+8518082 | NGC 188 | 15641.7, 16121.4, 16323.4, 16326.0, 16530.0 | 22 ± 5 | 16 ± 4 |
| 2M00441241+8509312 | NGC 188 | 15641.7, 16323.4, 16326.0, 16530.0, 16741.2, 16744.7 | 15 ± 1 | 17 ± 4 |
| 2M00320079+8511465 | NGC 188 | 15641.7, 16121.4, 16326.0, 16530.0 | 12 ± 2 | 13 ± 2 |
| 2M00465966+8513157 | NGC 188 | 15641.7, 16530.0 | 12 ± 5 | 17 ± 5 |
| 2M00350924+8517169 | NGC 188 | 15641.7, 16121.4, 16530.0, 16744.7 | 12 ± 3 | 12 ± 1 |
| 2M00571844+8510288 | NGC 188 | 15641.7, 16121.4, 16530.0 | 12 ± 3 | 13 ± 0.3 |
| 2M00415197+8527070 | NGC 188 | 15641.7, 16121.4, 16323.4, 16530.0 | 12 ± 4 | 12 ± 1 |
| 2M00445253+8514055 | NGC 188 | 15641.7, 16121.4, 16323.4, 16326.0, 16530.0 | 9 ± 2 | 10 ± 3 |
| 2M00581691+8540183 | NGC 188 | 15641.7, 16121.4, 16323.4, 16326.0, 16530.0 | 8 ± 1 | 7 ± 2 |
| 2M00463920+8523336 | NGC 188 | 15641.7, 16121.4, 16326.0, 16530.0, 16744.7 | 6 ± 0.9 | 8 ± 2 |
| 2M05114795+4740258 | NGC 1798 | 15641.7, 16121.4, 16323.4, 16326.0, 16530.0, 16741.2, 16744.7 | 14 ± 1 | 15 ± 3 |
| 2M06153140−1842562 | NGC 2204 | 15641.7, 16121.4, 16326.0, 16530.0, 16744.7 | 13 ± 2 | 12 ± 1 |
| 2M06145845−1838429 | NGC 2204 | 15641.7, 16121.4, 16323.4, 16326.0, 16327.3, 16530.0 | 12 ± 3 | 11 ± 2 |
| 2M06153666−1846527 | NGC 2204 | 15641.7, 16121.4, 16323.4, 16326.0, 16530.0 | 11 ± 2 | 11 ± 1 |
| 2M07381507+2134589 | NGC 2420 | 15641.7, 16326.0, 16530.0, 16744.7 | 10 ± 0.5 | 10 ± 0.6 |
| 2M07382166+2133514 | NGC 2420 | 15641.7, 16530.0 | 7 ± 0.9 | 7 ± 0.1 |
| 2M08493465+1151256 | NGC 2682 | 15641.7, 16121.4, 16326.0, 16530.0, 16744.7 | 8 ± 0.9 | 8 ± 1 |
| 2M12240101−5807554 | NGC 4337 | 15641.7, 16323.4, 16530.0 | 13 ± 2 | 15 ± 4 |
| 2M19212437+3735402 | NGC 6791 | 16326.0, 16744.7 | 24 ± 4 | >18 ± 2 |
| 2M19213390+3750202 | NGC 6791 | 15641.7, 16327.3, 16530.0 | 12 ± 0.9 | 13 ± 3 |
| 2M19211606+3746462 | NGC 6791 | 15641.7, 16121.4, 16530.0, 16741.2, 16744.7 | 11 ± 0.8 | 11 ± 1 |
| 2M19213635+3739445 | NGC 6791 | 15641.7, 16121.4, 16744.7 | 10 ± 1 | >8 ± 1 |
| 2M19411705+4010517 | NGC 6819 | 15641.7, 16121.4, 16530.0, 16744.7 | 18 ± 3 | 15 ± 2 |
| 2M19411971+4023362 | NGC 6819 | 15641.7, 16121.4, 16530.0, 16744.7 | 13 ± 1 | 12 ± 2 |
| 2M19413439+4017482 | NGC 6819 | 15641.7, 16121.4, 16323.4, 16530.0, 16744.7 | 13 ± 2 | 13 ± 1 |
| 2M19412658+4011418 | NGC 6819 | 15641.7, 16323.4, 16530.0 | 8 ± 2 | 10 ± 2 |
| 2M23571013+5647167 | NGC 7789 | 16327.3 | 3 ± 0.7 | >6 |
| 2M23570744+5641417 | NGC 7789 | 15641.7, 16121.4, 16530.0, 16744.7 | 15 ± 1 | 17 ± 3 |
| 2M23555312+5641203 | NGC 7789 | 15641.7, 16121.4, 16323.4, 16326.0, 16530.0 | 9 ± 1 | 11 ± 3 |
| 2M23581471+5651466 | NGC 7789 | 15641.7, 16121.4, 16530.0 | 9 ± 0.9 | 10 ± 0.9 |
| 2M12400451−6036566 | Trumpler 20 | 15641.7, 16121.4, 16530.0 | 14 ± 4 | 15 ± 2 |
| 2M12390411−6034001 | Trumpler 20 | 15641.7, 16323.4, 16326.0, 16530.0 | 10 ± 2 | 10 ± 1 |
| 2M12402480−6043101 | Trumpler 20 | 15641.7, 16326.0 | 10 ± 3 | >10 ± 0.6 |
| 2M12400755−6035445 | Trumpler 20 | 15641.7, 16121.4, 16323.4, 16530.0 | 10 ± 0.9 | 10 ± 0.5 |
| 2M12400260−6039545 | Trumpler 20 | 15641.7, 16323.4, 16530.0 | 9 ± 2 | 10 ± 2 |
| 2M12391003−6038402 | Trumpler 20 | 15641.7, 16121.4, 16323.4, 16326.0, 16530.0 | 8 ± 3 | 11 ± 2 |
| 2M12402949−6038518 | Trumpler 20 | 15641.7, 16326.0, 16530.0 | 8 ± 3 | 11 ± 1 |
| 2M12385807−6030286 | Trumpler 20 | 15641.7, 16121.4, 16530.0 | 6 ± 3 | 8 ± 2 |
| 2M12392699−6036052 | Trumpler 20 | 15641.7 | 6 ± 1 | >9 |

range typical of each evolutionary group; see section 5.2.2 in Jönsson et al. (2020) for the specific values used to determine each group. We note that, due to the difficult nature of distinguishing between the early RGB and the RC, there are potential misclassifications. Therefore, these assigned evolutionary states should be taken as an approximation. Table 2 lists the evolutionary state for each star in our sample.

Though data for each cluster are sparse compared to the range of each Lagarde model shown, in general we see that the data line up with the models within the margin of error. Also in nearly every case, the RGB stars have higher $^{12}$C/$^{13}$C ratios than the clump stars, which is expected because clump stars have fully completed extra mixing on the RGB, while RGB stars have not.

### 3.2 $^{12}$C/$^{13}$C as a function of age and mass

We are also interested in how the $^{12}$C/$^{13}$C ratio and extra mixing change for stars of different ages or masses. The $^{12}$C/$^{13}$C ratios as a function of age and mass for our sample are presented in Figs 5

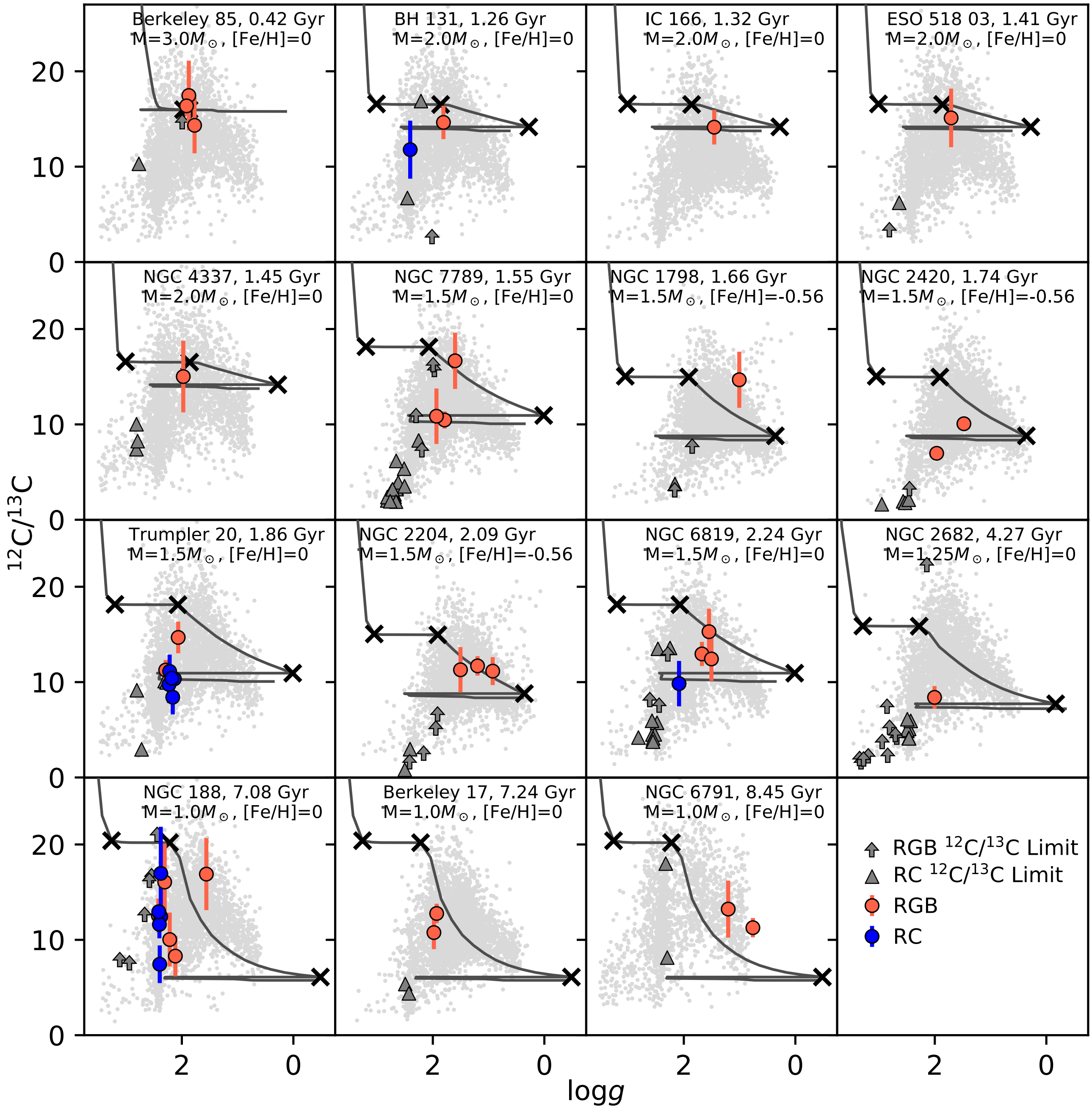

**Figure 4.** The evolution of the $^{12}$C/$^{13}$C ratio as a function of log $g$ for each cluster. Typical errors in log $g$ are 0.02 dex. *Blue circles* correspond to red clump (core He-burning) stars, and *orange circles* correspond to stars on the RGB. The Lagarde models are shown as *dark grey curves*, and the three *black* × symbols mark the end of the first dredge-up, the RGB luminosity bump, and the tip of the RGB (left to right) on each model. *Light grey points* represent field stars in the BAWLAS VAC that have $^{12}$C/$^{13}$C and [Fe/H] within 0.03 dex of each cluster mean [Fe/H]; we note that these field stars are not necessarily the same age as the cluster stars. *Dark grey arrows* are $^{12}$C/$^{13}$C limit stars belonging to each cluster.

and 6, respectively. Both figures display the $^{12}$C/$^{13}$C ratios from each individual star (left) and the mean $^{12}$C/$^{13}$C value for each cluster and evolutionary group (right), using the same evolutionary state colour conventions as previously described. We note that in the individual star measurement plots, the data points for a given cluster are offset in age or mass randomly, covering a small range around the true cluster age or mass to allow for better visualization of the error bars for a given star.

As shown in Fig. 5, the $^{12}$C/$^{13}$C scatter at a given age is reduced, when one accounts for the stellar evolutionary state (see left-hand panel of Fig. 5). For example, in the 1–2.5 Gyr range, two distinct groupings show the same decreasing trend in $^{12}$C/$^{13}$C with increasing age; however, the less evolved stars (shown as orange symbols) that are most likely still involved in thermohaline extra mixing on the RGB have slightly higher $^{12}$C/$^{13}$C ratios than the more evolved stars (blue symbols). Likewise, the $^{12}$C/$^{13}$C-mass relation exhibits a similar split between evolutionary groups in the 1.5–2 M$_\odot$ range with the less evolved RGB stars exhibiting the same trend with stellar mass as the more evolved stars, just offset to higher $^{12}$C/$^{13}$C ratios.

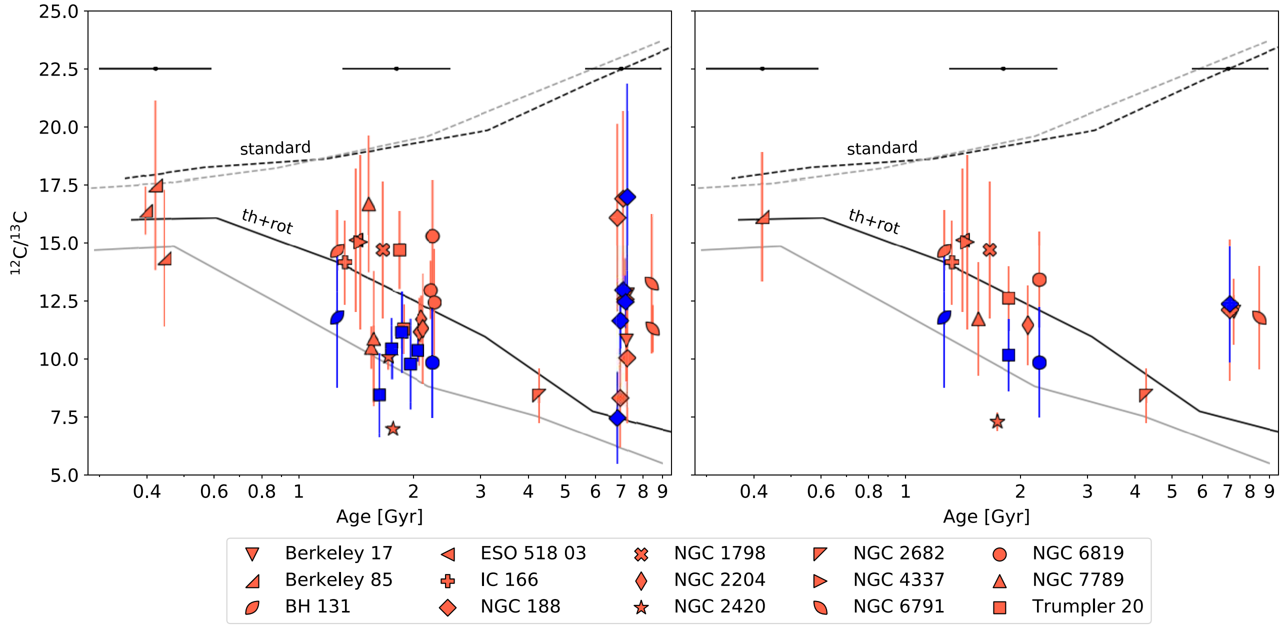

**Figure 5.** The $^{12}C/^{13}C$ ratio as a function of age for individual open cluster stars (*left*) and mean cluster values (*right*). *Blue data points* correspond to red clump stars undergoing core He-burning, and *orange data points* correspond to stars on the RGB. Individual stars in a given cluster, or at the same age, are intentionally offset slightly in age to better show the $^{12}C/^{13}C$ error bars. Horizontal, *black error bars* at the top of each figure represent typical age errors. Overlaid are curves showing the $^{12}C/^{13}C$ and age values at the tip of the RGB from the Lagarde models assuming: (1) standard stellar evolution (*dashed curves*), and (2) thermohaline mixing and stellar rotation (*solid curves*), for [Fe/H] = 0 (*black*) and [Fe/H] = -0.56 (*grey*).

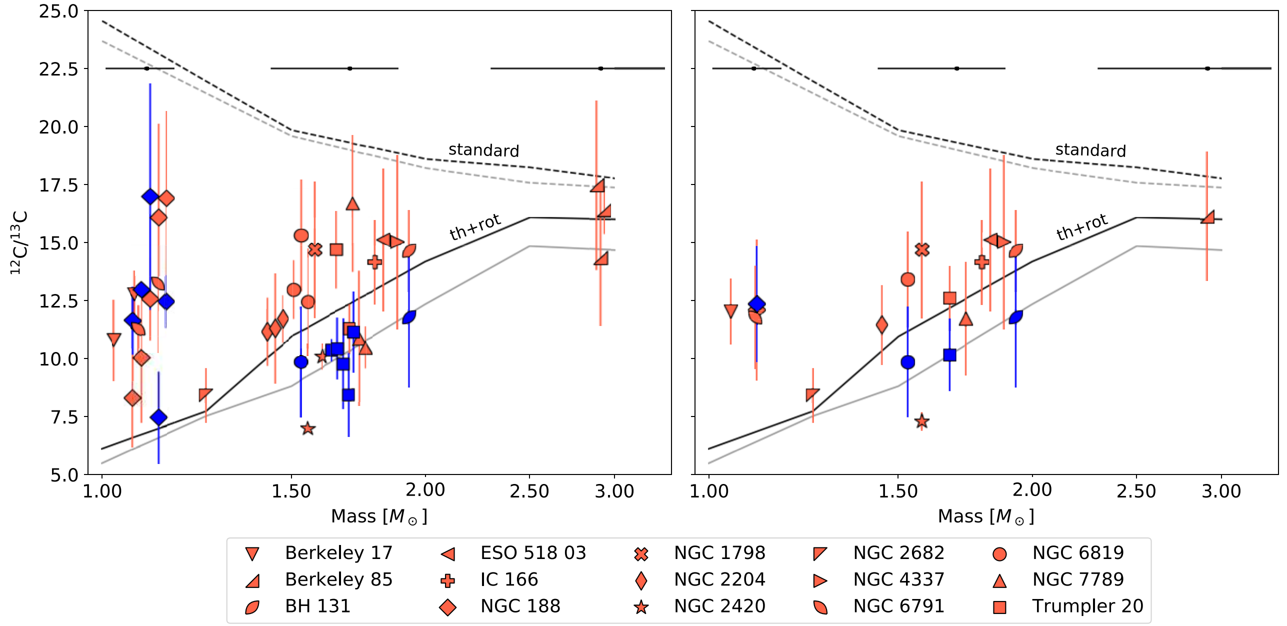

**Figure 6.** The same as Fig. 5, but as a function of the initial stellar mass for stars at the cluster main sequence turn off instead of stellar age. Horizontal, *black error bars* at the top of each figure represent typical mass errors.

Overlaying the data in Figs 5 and 6 are the Lagarde models that show the predicted $^{12}C/^{13}C$-age/mass trend for both the standard mixing theory (i.e. only convection; dashed curve) and one that includes extra mixing due to the thermohaline instability and stellar rotation (solid curve). The colours of the models indicate metallicity, where black is for [Fe/H] = 0 and grey is for [Fe/H] = −0.56. The models shown are the predicted $^{12}C/^{13}C$ values for stars at the tip of the RGB. Therefore, if stars with mass less than $\backsim 2.2 M_\odot$ experience thermohaline extra mixing, we expect the orange points to fall slightly above the extra mixing model, since these stars have not been mixed as much as the model; furthermore, the blue points should fall at or slightly below the extra mixing model, since these stars have undergone all of RGB thermohaline extra mixing, but could be slightly more mixed due to rotation.

We find that our data exhibit $^{12}$C/$^{13}$C values, consistently lower than the standard mixing model predictions, and have slight trends with age and mass, which implies a need for extra mixing on the RGB to explain these observations. The data agree more closely with the thermohaline and rotation model, though there are notable discrepancies, specifically toward the older/less-massive regime, that require further investigation and could provide useful information to improve our extra mixing understanding.

## 4 DISCUSSION

We have studied how the $^{12}$C/$^{13}$C ratio changes for red giants of varying evolutionary state and age/mass. Because these characteristics each affect extra mixing efficiency, drawing conclusions about the entire sample as a whole is difficult. Instead, we discuss here the $^{12}$C/$^{13}$C trends and uncertainties within subgroups of stars in our sample with similar characteristics.

First, the stars belonging to Berkeley 85 are predicted to have an initial mass of $2.91^{+0.43}_{-0.61}$ M$_{\odot}$ and have slightly super solar-metallicity ([Fe/H] = 0.10 ± 0.01). Stars with these parameters are not thought to reach the conditions for thermohaline mixing to occur since the non-degenerate He-core begins He-burning before the RGB bump can be reached (e.g. Charbonnel & Lagarde 2010; Lagarde et al. 2019). Therefore, the predominant mechanism for mixing in these stars is stellar rotation. The effect of stellar rotation slightly lowering the $^{12}$C/$^{13}$C on the RGB can be seen by comparing the standard model and the extra mixing model predictions at this age/mass in Figs 5 and 6.

Next, stars with initial mass below ∽2.2 M$_{\odot}$ (e.g. Charbonnel & Lagarde 2010; Lagarde et al. 2019) are expected to experience the conditions for thermohaline extra mixing. Moreover, thermohaline extra mixing is thought to be the dominating extra mixing mechanism for these stars on the RGB. In the 1–2.5 Gyr, or 1.5–2 M$_{\odot}$, range in Figs 5 and 6, we observe generally good agreement with the models. That is, most of the orange stars have $^{12}$C/$^{13}$C values higher than the model, since these stars have not undergone as much mixing as stars in the model have at the tip of the RGB, and the blue stars have $^{12}$C/$^{13}$C values at or lower than the model given $^{12}$C/$^{13}$C error bars, since these stars have undergone the full extent of RGB extra mixing.

Notably, in the 1–2.5 Gyr/1.5–2 M$_{\odot}$ range, there are three clusters that have subsolar metallicities that fall closer to the grey model (i.e. [Fe/H] = -0.56): NGC 1798, NGC 2420, and NGC 2204. Specifically for NGC 2420, these stars tend to have $^{12}$C/$^{13}$C values that fall more in line with the grey model. The lower metallicity, grey model predicts lower $^{12}$C/$^{13}$C values than the black model implying more mixing has occurred for these more metal-poor stars. However, from these data, it is uncertain if this is a general trend attributed to the metallicity of the star, since the stars in NGC 1798 and NGC 2204 have $^{12}$C/$^{13}$C values that are relatively similar to the near-solar metallicity stars and the black model. Additionally, there is always the question whether the stars in NGC 2420 are actually RC stars that have undergone the full extent of RGB extra mixing, which could explain the lower $^{12}$C/$^{13}$C values.

Finally, the clusters in the old, low-mass range (less than ∽1.25 M$_{\odot}$) exhibit notable deviations from the thermohaline model. Most of these stars show relatively high $^{12}$C/$^{13}$C values compared to the extra mixing model. Though unknown at present, these differences could possibly be due to: (1) systematics in our $^{12}$C/$^{13}$C measurements, (2) the need for more careful analysis of the evolutionary states, (3) the need for fine tuning of the extra mixing models so that they better match observations, or (4) some combination of these factors.

One obvious cluster that deviates from the thermohaline model in Figs 5 and 6 is NGC 188. This cluster exhibits relatively high $^{12}$C/$^{13}$C ratios for nearly all of its stars compared to the thermohaline model. Additionally, there are a few stars belonging to the cluster that have non-intuitive evolutionary state classifications and $^{12}$C/$^{13}$C ratios. Notably, the two RGB (orange) stars with low $^{12}$C/$^{13}$C (∽10) at log *g* ∽ 2 (see Fig. 4) are peculiar because they should not have experienced the luminosity bump and extra mixing, given their log *g* values if they are truly on the RGB, and yet they have such low $^{12}$C/$^{13}$C ratios. Similarly, one star classified as a RC star shows $^{12}$C/$^{13}$C ∽ 17, which is abnormally high for a star that should have fully undergone extra mixing.

We can only conjecture possible explanations for these anomalies. Perhaps these peculiar stars have been misclassified as NGC 188 members, or they are members misclassified as RGB or RC and are actually in some other phase of evolution, such as the AGB. Alternatively, there could be some missing dependency of extra mixing, such as a spread in stellar rotation speeds and mixing efficiencies, that we are not directly considering that could provide an explanation for these unexpected results. NGC 188 presents itself as an interesting case study, as it provided the largest number (10) of stars with reliably determined $^{12}$C/$^{13}$C ratios for a single cluster in this study, and the cluster seems to show a large intrinsic spread in these $^{12}$C/$^{13}$C ratios for both the RGB and RC evolutionary states, that are not well explained by either the standard or thermohaline model.

The data presented here cover a large range of stellar characteristics which affect RGB extra mixing, making it difficult to attribute just one model to explain all of the $^{12}$C/$^{13}$C observations. The Lagarde thermohaline and rotation models do a sufficient job for some of the data. There have been concerns raised in the literature, however, about modelling the thermohaline instability to explain RGB extra mixing in general, and if this instability is physically able to cause a large-scale change in surface abundances (e.g. see Tayar & Joyce 2022 and references therein). Most notably, hydrodynamical simulations (e.g. Denissenkov 2010, Denissenkov & Merryfield 2011, Traxler, Garaud & Stellmach 2011) have yielded short, wide ‘salt fingers’ that transport material, meaning the so-called C parameter, which is related to the ratio of the salt finger’s length to diameter, is on the order of 1 to a few (Kippenhahn, Ruschenplatt & Thomas 1980). For the thermohaline instability to reach the convective envelope of the star, one needs to incorporate long, thin salt fingers; often a C value on the order of 1000 is adopted to ensure the instigation of these long fingers, and extra mixing with the envelope (e.g. Ulrich 1972, Charbonnel & Zahn 2007). This large difference in C causes some to question our understanding of the thermohaline instability in RGB stars and its ability to explain extra mixing.

Incorporating multiple physical processes, such as thermohaline instability and stellar rotation as in the case of the Lagarde models, is one way that authors have been able to fine tune the models to produce the observed abundances. However, like some other studies attempting to model extra mixing, the Lagarde models have treated the thermohaline mixing and rotation-induced mixing independently and then simply added their effects, whereas these two processes may well interact in a real system, affecting how each process evolves. Studies incorporating interacting extra mixing processes are not widely available yet, though there have been attempts thus far (e.g. Maeder et al. 2013; Sengupta & Garaud 2018). In the future, these models will ideally shed more light on to the mixing conditions in red giants.

## 5 CONCLUSIONS

We have investigated non-canonical, extra mixing in red giant stars by observing how the $^{12}$C/$^{13}$C ratio, a tracer of red giant internal mixing, evolves on the RGB, and we have studied how this chemical evolution varies with stellar age and mass. To do so, we first isolated a sample of 43 red giant stars, reliably identified as belonging to one of 15 surveyed open clusters, from the APOGEE DR17 data set that have $^{12}$C/$^{13}$C ratios derived as a part of the BAWLAS VAC (Hayes et al. 2022). We then identified the evolutionary state of each star using the APOGEE RGB/RC flags. Finally, to test the overall importance of extra mixing in predicting red giant surface abundances and to gain insight into its instigator, we compared how the $^{12}$C/$^{13}$C ratios varied with evolutionary state, age, and mass to how they are expected to vary based on two theoretical models: (1) standard stellar evolution (i.e. no extra mixing on the RGB) and (2) RGB extra mixing (in this case, we used the thermohaline and stellar rotation Lagarde model). Our results are highlighted in Figs 4, 5, and 6.

While the details of thermohaline mixing are still debated, our data set of red giant stars with varying mass, evolutionary state, and homogeneously derived $^{12}$C/$^{13}$C show a clear need for extra mixing of some form along the RGB. We find that the $^{12}$C/$^{13}$C in stars with mass greater than ∽2.5 $M_{\odot}$ can be explained by stellar rotation since thermohaline extra mixing is not expected to occur in these stars. Additionally, we find that the Lagarde models do a reasonable job of matching the general trends exhibited by the observations and suggest that the source of extra mixing must produce similar trends. Specifically, $^{12}$C/$^{13}$C tends to decrease with increasing age or decreasing mass in the age/mass range 1–2 Gyr/1.5–2 $M_{\odot}$. From these data, the $^{12}$C/$^{13}$C likely decreases more, or mixing is more efficient, for lower metallicity stars at a given age/mass in this range. Finally, stars in our data set less massive than ∽1.25 $M_{\odot}$ tend to deviate from model predictions, so either additional, detailed observations and analyses are needed to justify this trend or the thermohaline model prescription needs to be revised to explain these observed mixing indicators. The growing availability of similar high-quality data will ultimately help constrain the physics of extra mixing, and inform how to accurately model what is happening in stellar interiors during these dramatic events.

## ACKNOWLEDGEMENTS

CM, SRM, and AA acknowledge support from National Science Foundation grant no. AST-1909497.

TM acknowledges financial support from the Spanish Ministry of Science and Innovation (MICINN) through the Spanish State Research Agency, under the Severo Ochoa Program 2020–2023 (CEX2019-000920-S), as well as support from the ACIISI, Consejería de Economía, Conocimiento y Empleo del Gobierno de Canarias, and the European Regional Development Fund (ERDF) under grant no. with reference PROID2021010128.

Funding for SDSS-IV has been provided by the Alfred P. Sloan Foundation, the U.S. Department of Energy Office of Science, and the participating institutions.

SDSS-IV acknowledges support and resources from the Center for High Performance Computing at the University of Utah. The SDSS website is www.sdss.org.

SDSS-IV is managed by the Astrophysical Research Consortium for the participating institutions of the SDSS collaboration including the Brazilian Participation Group, the Carnegie Institution for Science, Carnegie Mellon University, Center for Astrophysics, Harvard and Smithsonian, the Chilean Participation Group, the French Participation Group, Instituto de Astrofísica de Canarias, the Johns Hopkins University, Kavli Institute for the Physics and Mathematics of the Universe (IPMU)/University of Tokyo, the Korean Participation Group, Lawrence Berkeley National Laboratory, Leibniz Institut für Astrophysik Potsdam (AIP), Max-Planck-Institut für Astronomie (MPIA Heidelberg), Max-Planck-Institut für Astrophysik (MPA Garching), Max-Planck-Institut für Extraterrestrische Physik (MPE), National Astronomical Observatories of China, New Mexico State University, New York University, University of Notre Dame, Observatário Nacional/MCTI, The Ohio State University, Pennsylvania State University, Shanghai Astronomical Observatory, United Kingdom Participation Group, Universidad Nacional Autónoma de México, University of Arizona, University of Colorado Boulder, University of Oxford, University of Portsmouth, University of Utah, University of Virginia, University of Washington, University of Wisconsin, Vanderbilt University, and Yale University.

## DATA AVAILABILITY

The data underlying this article were accessed from SDSS DR17 (Abdurro'uf et al. 2022). The derived data generated in this research will be shared on reasonable request to the corresponding author.

## REFERENCES

Abdurro'uf et al., 2022, ApJS, 259, 35
Allende Prieto C., Beers T. C., Wilhelm R., Newberg H. J., Rockosi C. M., Yanny B., Lee Y. S., 2006, ApJ, 636, 804
Beaton R. L. et al., 2021, AJ, 162, 302
Blanton M. R. et al., 2017, AJ, 154, 28
Boothroyd A. I., Sackmann I. J., 1999, ApJ, 510, 232
Boothroyd A. I., Sackmann I. J., Wasserburg G. J., 1995, ApJ, 442, L21
Bossini D. et al., 2019, A&A, 623, A108
Bowen I. S., Vaughan A. H. J., 1973, Appl. Opt., 12, 1430
Brogaard K. et al., 2021, A&A, 649, A178
Busso M., Wasserburg G. J., Nollett K. M., Calandra A., 2007, ApJ, 671, 802
Cantat-Gaudin T. et al., 2020, A&A, 640, A1
Chanamé J., Pinsonneault M., Terndrup D. M., 2005, ApJ, 631, 540
Charbonnel C., 1995, ApJ, 453, L41
Charbonnel C., Lagarde N., 2010, A&A, 522, A10
Charbonnel C., Zahn J. P., 2007, A&A, 467, L15
Charbonnel C. et al., 2020, A&A, 633, A34
Choi J., Dotter A., Conroy C., Cantiello M., Paxton B., Johnson B. D., 2016, ApJ, 823, 102
Denissenkov P. A., 2010, ApJ, 723, 563
Denissenkov P. A., Merryfield W. J., 2011, ApJ, 727, L8
Denissenkov P. A., Pinsonneault M., MacGregor K. B., 2009, ApJ, 696, 1823
Dias W. S., Alessi B. S., Moitinho A., Lépine J. R. D., 2002, A&A, 389, 871
Donor J. et al., 2018, AJ, 156, 142
Donor J. et al., 2020, AJ, 159, 199
Dotter A., 2016, ApJS, 222, 8
Drazdauskas A., Tautvaišienė G., Randich S., Bragaglia A., Mikolaitis Š., Janulis R., 2016, A&A, 589, A50
Frinchaboy P. M. et al., 2013, ApJ, 777, L1
García Pérez A. E. et al., 2016, AJ, 151, 144
Gilroy K. K., 1989, ApJ, 347, 835
Gratton R. G., Sneden C., Carretta E., Bragaglia A., 2000, A&A, 354, 169
Gunn J. E. et al., 2006, AJ, 131, 2332
Gustafsson B., Edvardsson B., Eriksson K., Jørgensen U. G., Nordlund Å., Plez B., 2008, A&A, 486, 951
Hayes C. R. et al., 2022, ApJS, 262, 34
Holtzman J. A., Harrison T. E., Coughlin J. L., 2010, Adv. Astron., 2010, 193086
Holtzman J. A. et al., 2015, AJ, 150, 148
Jönsson H. et al., 2020, AJ, 160, 120

Kippenhahn R., Ruschenplatt G., Thomas H. C., 1980, A&A, 91, 175
Lagarde N., Decressin T., Charbonnel C., Eggenberger P., Ekström S., Palacios A., 2012, A&A, 543, A108
Lagarde N. et al., 2019, A&A, 621, A24
Maeder A., Meynet G., Lagarde N., Charbonnel C., 2013, A&A, 553, A1
Majewski S. R. et al., 2017, AJ, 154, 94
Masseron T., Merle T., Hawkins K., 2016, Astrophysics Source Code Library, record ascl:1605.004
Myers N. et al., 2022, AJ, 164, 85
Nidever D. L. et al., 2015, AJ, 150, 173
Palacios A., Talon S., Charbonnel C., Forestini M., 2003, A&A, 399, 603
Palacios A., Charbonnel C., Talon S., Siess L., 2006, A&A, 453, 261
Paxton B., Bildsten L., Dotter A., Herwig F., Lesaffre P., Timmes F., 2011, ApJS, 192, 3
Paxton B. et al., 2013, ApJS, 208, 4
Paxton B. et al., 2015, ApJS, 220, 15
Paxton B. et al., 2018, ApJS, 234, 34
Sackmann I. J., Boothroyd A. I., 1999, ApJ, 510, 217
Santana F. A. et al., 2021, AJ, 162, 303
Sengupta S., Garaud P., 2018, ApJ, 862, 136
Shetrone M. et al., 2015, ApJS, 221, 24
Smiljanic R., Gauderon R., North P., Barbuy B., Charbonnel C., Mowlavi N., 2009, A&A, 502, 267
Smith V. V. et al., 2021, AJ, 161, 254
Sneden C., Pilachowski C. A., Vandenberg D. A., 1986, ApJ, 311, 826
Stern M. E., 1960, Tellus, 12, 172
Sweigart A. V., Mengel J. G., 1979, ApJ, 229, 624
Szigeti L. et al., 2018, MNRAS, 474, 4810
Takeda Y., Omiya M., Harakawa H., Sato B., 2019, PASJ, 71, 119
Tautvaišienė G., Edvardsson B., Puzeras E., Barisevičius G., Ilyin I., 2010, MNRAS, 409, 1213
Tautvaišienė G., Barisevičius G., Chorniy Y., Ilyin I., Puzeras E., 2013, MNRAS, 430, 621
Tayar J., Joyce M., 2022, ApJ, 935, L30
Traxler A., Garaud P., Stellmach S., 2011, ApJ, 728, L29
Ulrich R. K., 1972, ApJ, 172, 165
Wasserburg G. J., Boothroyd A. I., Sackmann I. J., 1995, ApJ, 447, L37
Wilson J. C. et al., 2019, PASP, 131, 055001
Zasowski G. et al., 2013, AJ, 146, 81
Zasowski G. et al., 2017, AJ, 154, 198

This paper has been typeset from a TEX/LATEX file prepared by the author.